Metallurgical and Materials Applications of
Shock-Wave and High-Strain-Rate Phenomena
L.E. Murr, K.P. Staudhammer and M.A. Meyers (Editors)

166

58

High-strain, high-strain-rate deformation of tantalum: the thick-walled cylinder method

M.A. Meyers [ab], V.F. Nesterenko [bc], Y.J. Chen [b], J.C. LaSalvia [ab], M.P. Bondar [c], and Y.L. Lukyanov [c]

[a] Institute for Mechanics and Materials

[b] Department of Applied Mechanics and Engineering Sciences, UC San Diego
La Jolla, California, 92093 U.S. A.

[c] Lavrentyev Institute of Hydrodynamics, Russian Academy of Sciences, Novosibirsk, Russia

Tantalum was subjected to high plastic strains (shear strains, γ up to 10) at high strain rates (~ 10^4 s^{-1}) by the collapse of a thick-walled cylinder. The strains and temperatures were computed as a function of distance from the cylinder axis. The microstructural features were: (i) dislocations and elongated cells *($\gamma < 2$, $T < 600$ K)*; (ii) subgrains *($2 < \gamma < 6$, $600\ K < T < 800\ K$)*; (iii) dynamically recrystallized micrograins *($6 < \gamma < 8$, $800\ K < T < 900\ K$)*; and (iv) static recrystallized grains *($\gamma > 10$, $T > 1000$ K)*. Grain-scale localization produced by anisotropic plastic flow and localized recovery and recrystallization were observed at plastic strains *$\gamma > 4$*. Ductile fracturing along shear localization bands was produced by the residual tensile hoop stresses generated near the central hole region upon unloading.

1. INTRODUCTION

Tantalum and tantalum-tungsten alloys are attractive for chemical-energy penetrators (shaped charges and EFP's) because of their high density (ρ ~ 16.7 x $10^3 kg/m^3$) and considerable ductility and strength. In EFP's the effective plastic strains can reach levels of up to 10 [1, 2], whereas in shaped charges they can be even higher. Characterization and analysis of the microstructural changes have been carried out by Murr and co-workers on recovered shaped-charge [3,4] and EFP [5,6] specimens. They observed a broad range of microstructures: dislocation cells, sub-boundaries, and recrystallized grains. The thermomechanical conditions experienced by shaped charges and EFP's can be simulated with experiments using hat-shaped specimens and thick-walled cylinders. The hat-shaped specimen, developed by Meyer and Manwaring [7], has recently been applied to tantalum [8]. The limitation of this technique is that the effective strain achieved not higher than ~3. The primary microstructural changes observed were dynamic recovery and the onset of dynamic recrystallization within isolated regions, due to heterogeneous plastic flow. The calculated mean temperature was 800 K, insufficient to global dynamic recrystallization. The thick-walled cylinder method, developed by Nesterenko and coworkers [9, 10], enables the generation of higher plastic strains under controlled conditions. This report describes the application of this technique to tantalum, its microstructural changes, and correlates them with the local thermal excursion.

2. EXPERIMENTAL PROCEDURE

Two types of tantalum (Cabot Co.) were used in this research:

a) Disks (8 mm thick). This material was received as a 155 mm diameter disk; the processing and structure are described in detail by Meyers et al. [8]. The grain size is 31 μm. The principal interstitial contents are C: 60; 0: 70; N: 10; H: 4, in parts per million.

b) Tubes Tantalum tubes, with an internal diameter of 15 mm. The grain size is 39 μm. The principal interstitial contents are C: 25; 0: 60; N: <10; H: <5, in parts per million.

Tantalum disks and tube were incorporated into a copper thick-walled cylinder to form a portion of the internal wall. Figure 1 shows the schematic of the experimental configuration used. The tubular specimen was placed in the center. The external radius of the specimens is 9.5 mm and the internal radius is 5.5 mm for disk specimens and 7.5 mm for tubes. The final internal radius of Ta can be taken as zero. The strain rate as a function of time varies between 1 and 3.5 x 10^4 s^{-1} during the collapse process. This process has been described in detail by Nesterenko et al. [9].

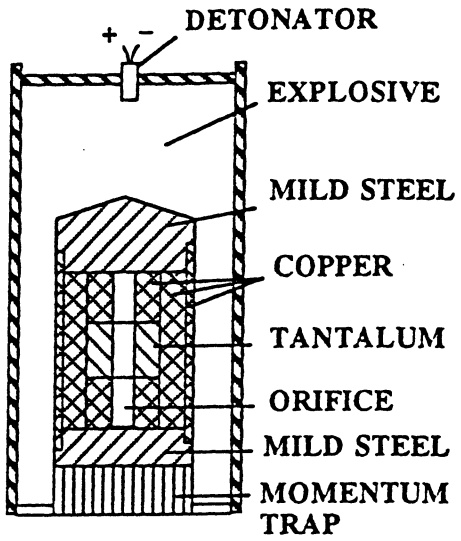

Figure 1. Experimental setup.

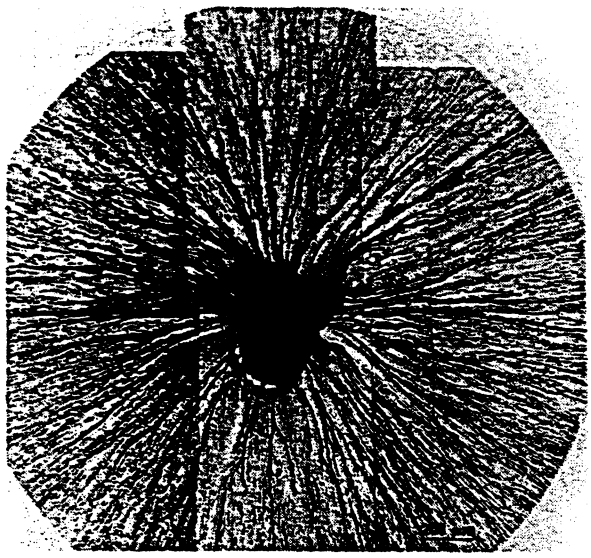

Figure 2. Detail of collapsed cylinder showing residual central hole and radial cracks.

3. RESULTS AND DISCUSSION

3.1. Overall Microstructural Changes

The center of the collapsed tantalum cylinder (tube) is shown in Figure 2. The central orifice with a radius of ~ 0.5 mm is due to either jetting along the cylinder axis or to the insufficient energy for collapse. A pattern of convergent plastic flow and radial cracks along shear localized regions can be seen. Figure 3 shows a broad variety of microstructural features near the central orifice region. There is a reduction in grain size from the initial value of 31 μm to 17 μm in the well-annealed regions near the central orifice; this is indicative of recrystallization. The grain size decreases as a function of distance from the internal surface. Figure 4 shows the recrystallized grain size as a function of distance. Two distinct areas can be seen: uniformly etched regions at the front of the cracks, marked R in Figure 3(a); elongated features marked E in Figure 3(b). The crack tips show considerable blunting and a radius of ~10 μm. This is indicative of ductile response of tantalum. Microhardness measured radially exhibited the consistency with the microstructural changes (Figure 5). The hardness is higher in the uniformly etched region (R). This is clear in Figure 5(a). In Figure 5(b) two regions were characterized: distinct bands of concentrated deformation (A) and regions in which the grains were less distorted (B). There is a clear difference between the two. This will be discussed again in Figure 10.

Meyers et al. [8] determined the a quasi-static (10^{-3} s^{-1}) flow stress of 300 MPa for the tantalum disk, consistently with the initial hardness of HVN 100, which corresponds to 980 MPa (980/3 = 326). Although as-received tantalum is somewhat work-hardened and therefore the yield stress exceeds the predicted Hall-Petch value for grain size of 31 μm, it is possible to estimate the grain size for the areas R, having the hardness of HVN 200 (1960 MPa), by using Hall-Petch parameters for tantalum given by Armstrong [11] and Zerilli and Armstrong [12]:

Figure 3. (a)Microstructure in vicinity of central hole and cracks; (b) detail of crack tip; note absence of elongated marks ahead of crack tips.

$$\sigma = \sigma_o + kd^{-1/2} \quad (1)$$

where $90 \leq \sigma_o \leq 210$ MPa and $9 \leq k \leq 19$ MPa/mm$^{1/2}$. The predicted grain size is ~0.1 μm, obtained by taking k = 14 MPa mm$^{1/2}$.

Figures 6-9 show the microstructure evolution from dislocation cells, to sub-grains, and finally, to recrystallized grains. The misorientations between the elongated cells from region at ~1.5 mm from central axis were measured to be 2°, 6°, 4°, and 3.5° with respect to cell 1 (Figure 6). This is typical of a highly deformed structure ($\varepsilon_{ef} \cong 2$). A similar microstructure was observed by Murr et al. [5] on recovered tantalum EFP's, by Qiang et al. [2], and Wittman et al. [13]. The width of these cells is approximately 0.1 - 0.3 μm. Murr et al. [5] and Qiang et al. [2] measured misorientations varying between 3° and 8°. As the plastic deformation increases,

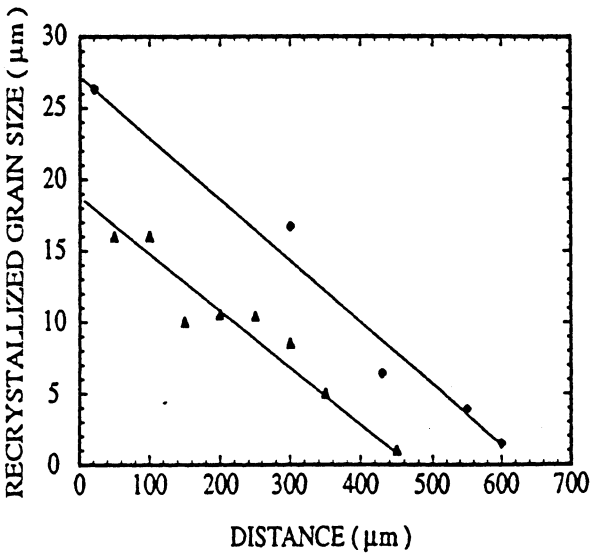

Figure 4. Recrystallized grain size as a function of distance from the central axis in collapsed cylinder.

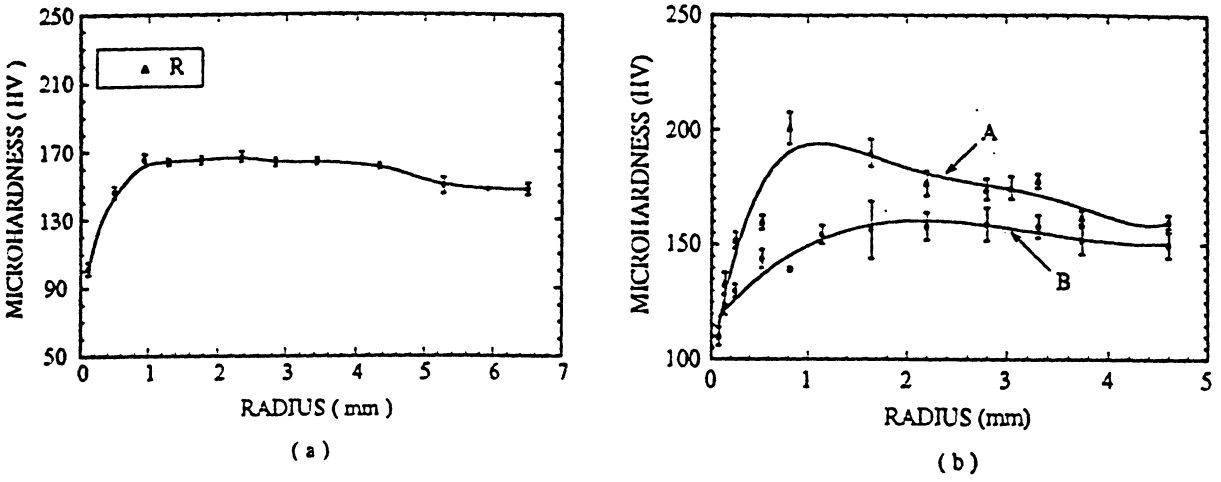

Figure 5. Microindentation hardness as a function of distance from the central axis of collapsed cylinder; (a) disk specimens; (b) tube specimens.

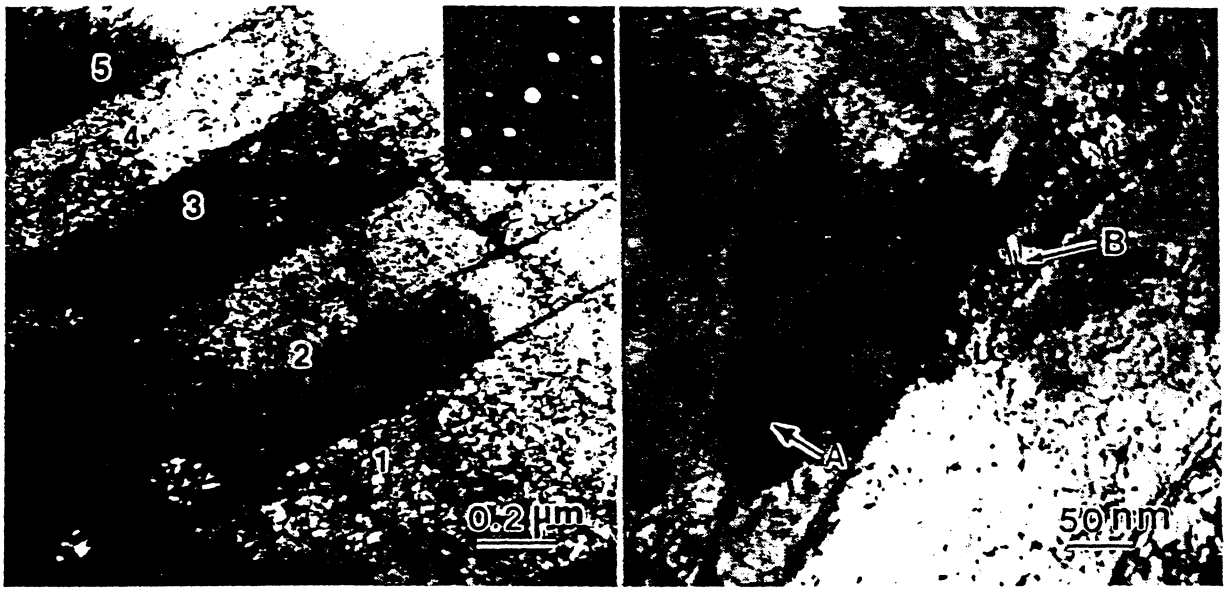

Figure 6. Transmission electron micrograph from region ~1.5 mm from central axis (effective strain: ~1.8; ΔT ~400 K); and [1 $\bar{1}$ 1] diffraction pattern from cell 4.

Figure 7. Transmission electron micrograph from region approximately 1.5 mm from central axis showing break-up of elongated sub-grains.

the misorientation between adjacent cells increases and the cell walls become sharper. A similar breakup pattern was observed by Andrade et al. [14] for copper. The long sub-grains break up into grains having a more equiaxed structure with the diameter equal to the width of the elongated sub-grains (~ 0.1 μm), which is in agreement with Hall-Patch prediction above. The mechanism of rotation recrystallization, defined by Derby [15] corresponds, approximately, to this process. Gil Sevillano et al. [16] suggested this mechanism to be a

characteristic feature of high-strain deformation. A small grain, in the process of formation, can be seen in Figure 7. It is indicated by an arrow A. The arrow B indicates Moiré fringes

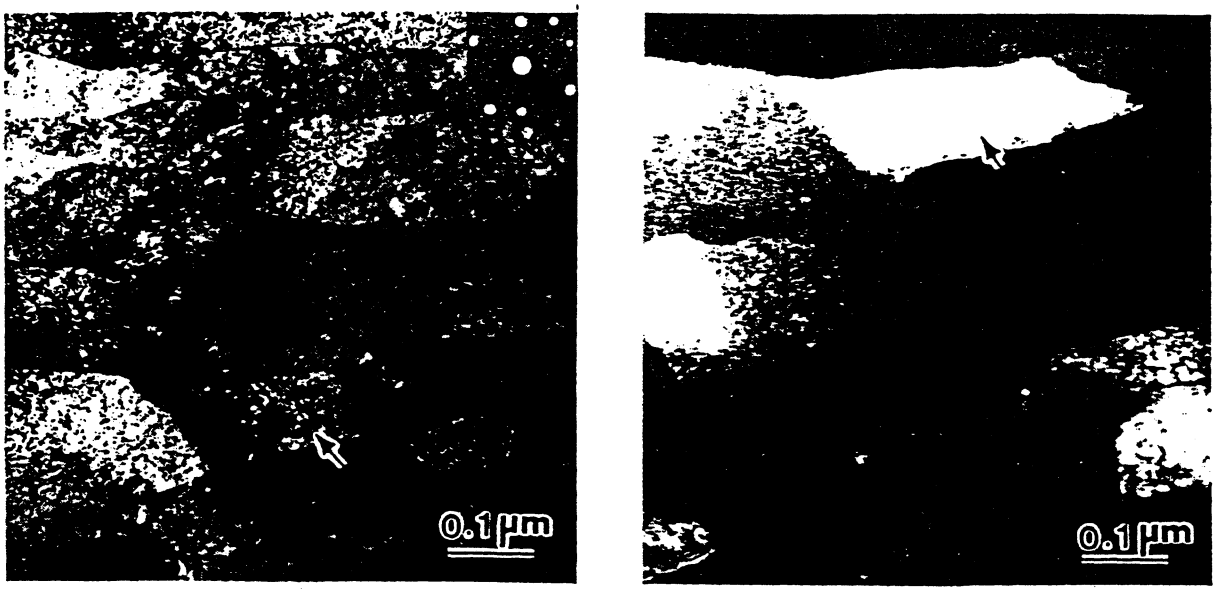

Figure 8. Transmission electron micrograph of region close (< 0.5mm) to central axis showing recrystallized structure; (a) bright field and diffraction pattern; and (b) dark field.

from the boundaries between adjacent grains; these fringes suggest that the boundaries are sharp and well defined, and that they are no longer composed of dislocations. In Figure 8 the microstructure becomes decidedly broken down into micrograins with an aspect ratio of ~ 2-3 and a width of ~0.1μm. The boundaries become clearly defined and the grains with less deformation are juxtaposed with highly deformed grains. The dark field image shows this very clearly.

3.2. Prediction of Strain and Temperature

The strain in the cylinder can be computed as a function of the initial dimensional parameters [8]. For the specific dimensional parameters of the current experiments (internal radii of 5.5 and 7.5 mm for the disk and tubular specimens, respectively) the effective strains as a function of distance from the cylinder axis are given in Figure 9(a). The dashed line represents a hypothetical experiment for which the initial radius of the inner wall is 40 mm. Effective plastic strains in the range 4 - 10 can be achieved by this deformation method.

The application of a modified Johnson-Cook constitutive equation with parameters provided by independent quasi-static and dynamic uniaxial compression tests is described by Meyers et al. [8]. The equation is expressed as:

$$\sigma = \left(\sigma_o + B\varepsilon^n\right)\left[1 + C\log\left(\dot{\varepsilon}/\dot{\varepsilon}_o\right)\right]e^{-\lambda(T-T_t)} \qquad (2)$$

The temperature rise as a function of strain becomes (assuming 90% conversion of plastic work into heat):

$$T = T_r + \frac{1}{\lambda} \ln\left[e^{\lambda(T_0 - T_r)} + \left(\frac{0.9\lambda\varepsilon}{\rho C_p}\right)\left[1 + C\log\left(\dot{\varepsilon}/\dot{\varepsilon}_0\right)\right]\left(\sigma_0 + \frac{B}{n+1}\varepsilon^n\right)\right] \quad (3)$$

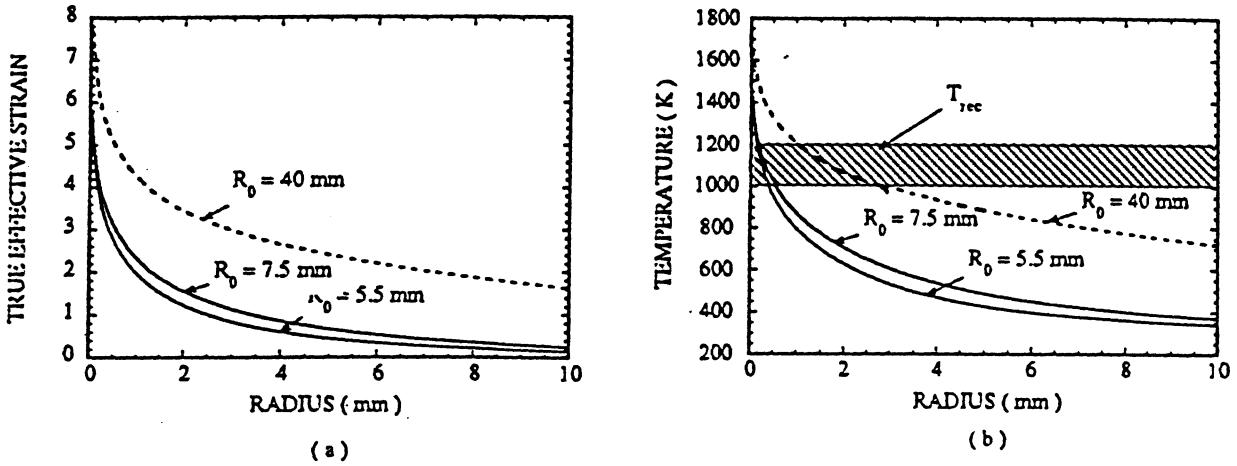

Figure 9 (a) Effective strain and (b) temperature as a function of distance from central axis for total collapse of tantalum cylinder.

The results are shown in Figure 9(b). The calculation was conducted for a strain rate of ~ 4 x 10^4 s^{-1}, which characterizes well the strain rate experienced by the inner wall of the cylinder. The range of recrystallization temperatures is marked in Figure 9(b). This range is estimated from literature: 1200 - 1500 K by Köck and Paschen [17]; 1000 K by Beckenhauer et al. [18] at ultra-rapid heating (803K/s) of high purity tantalum specimen. The conditions experienced by the dynamically deformed specimens resemble the ones simulated by Beckenhauer et al. [19] and this value is therefore taken as a lower bound for recrystallization. The results of the optical microscopy are entirely consistent with the temperature predictions of Figure 9(b). A recrystallized layer with a width of ~ 0.5 mm is clearly seen, (Figure 3) and this corresponds to the lower hardness region in Figure 5 and to the region whose temperature approaches the recrystallization temperature in Figure 9(b).

3.3. Localization of Plastic Deformation

The peculiar feature of Ta behavior is that plastic deformation being localized in separate regions (E) is accompanied by grains which are uniformly deformed with subsequent difference in microhardness (Figure 10). The formation of highly deformed bands juxtaposed with less deformed bands with increasing the plastic strain confirms earlier observations by Qiang et al. [2]. These highly deformed bands provide thermal fluctuations, which create periodic array of softened regions. Upon unloading, the residual tensile stresses produce opening

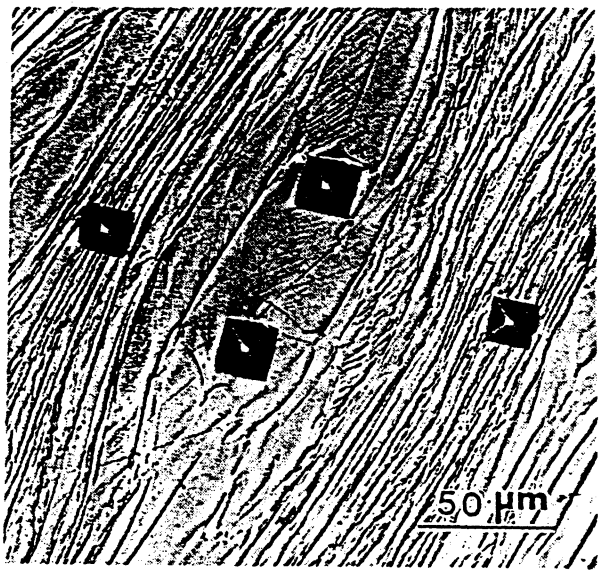

Figure 10. Microindentation markings showing evidence for grain-scale localization.

along these bands, and the cracks serve as markers for them (Figure 2). According to a plasticity analysis [19], after unloading, the residual tangential stress near the central orifice is tensile, becoming compressive at a radius of ~3.4 mm. This is an upper bound of the length estimated for mode I type cracks, and is in accord with the length of the cracks observed (Figure 3). The following aspects are relevant: a) Crack length: ~ 0.5 mm; b) Crack orientation: the radial trajectories of the cracks.

Vandermeer and Snyder [20] and Mitchell and Spitzig [21] found profound differences in work hardening for monocrystal Ta with different crystal orientations, which can lead to grain-scale localization in conjunction with texture softening. Texture softening becomes operative through plastic deformation due to the rotation of the grains towards orientations with larger Schmid factors. Asaro [22] showed that localization of plastic deformation can occur for crystals undergoing multiple shear with positive work hardening. Gil Sevillano et al. [16] discuss the heterogeneity of plastic deformation at high strains, and Meyers et al. [23] included textural softening in their classification of microstructural initiation sites for localization.

The material is under triaxial compression during the collapse of the cylinder and individual grains undergo very large extensions due to the pure shear imparted to them. Under the action of the compressive hoop stresses, the "softer" grains will deform more, and this can lead to much more pronounced grain distortions. Thus, grain-scale inhomogeneity of plastic deformation (texture softening and anisotropy of plastic flow) is thought to be the leading cause for localization of plastic deformation in tantalum deformed at high strain rates.

4. CONCLUSIONS

1. In the collapse of a thick-walled cylinder the plastic strain increases exponentially as the symmetry axis of the cylinder is approached. This technique enables controlled and reproducible plastic strains, at strain rates of the order of $4 \times 10^4 s^{-1}$.

2. The microstructure was observed to evolve in the following sequence: dislocations and dislocation cells for $\gamma < 2$; sub-grains (dynamic recovery) for $2 < \gamma < 6$; micrograins (dynamic recrystallization) for $6 < \gamma < 10$; and large equiaxed grains (static recrystallization) for $\gamma > 10$. This evolution is entirely consistent with the temperature rise predictions using a constitutive equation and experimental observation by Meyers et al. [8].

3. Profuse ductile cracks were observed propagating outward radially along the bands of highly deformed material. These cracks are produced by residual tensile tangential stresses in unloading stage.

4. The plastic deformation becomes heterogeneous after a critical strain with the formation of localization on the grain scale. This localization is due to texture softening and to the anisotropy of flow stress. The resulting temperature fluctuation, generating the radial paths of softened material, enhances the localization.

Acknowledgement: This research was supported by the US Army Research Office, University Research Initiative Program (contract DAAL-03-92-60108), by ARO Contract DAAH 04-93-G-0261, and by the National Science Foundation Institute for Mechanics and Materials.

REFERENCES

1. M.J. Worswick, N. Qiang, P. Niessen, and R.J. Pick, in "Shock-Wave and High-Strain-Rate Phenomena in Materials," M.A. Meyers, L.E. Murr, and K.P. Staudhammer, (eds.) M. Dekker, 1992, p.87.

2. N. Qiang, P. Niessen, and R.J. Pick, Mat. Sci. and Eng., A160 (1993) 49.
3. A.C. Gurevitch, L.E. Murr, H.K. Shih, C.S. Niou, A.H. Advani, D. Manuel, and L. Zernow, Mater. Charact., 30 (1993) 201.
4. H.K. Shih, C.-S. Niou, L.E. Murr, and L. Zernow, Scripta Met. et Mat., 29 (1993) 1291.
5. L.E. Murr, C.-S. Niou, and C. Feng, Scripta Met. et Mat., 31 (1994) 297.
6. L.E. Murr, H.K. Shih, and C.-S. Niou, Mater. Charact., 33 (1994) 65.
7. L.W. Meyer and S. Manwaring, in "Metallurgical Applications of Shock-Wave and High-Strain-Rate Phenomena," eds. L.E. Murr, K.P. Staudhammer, and M.A. Meyers, M. Dekker, NY, 1986, p. 657.
8. M.A. Meyers, Y.-J. Chen, F.D.S. Marquis, and D. S. Kim, Met. and Mat. Trans, September 1995.
9. V.F. Nesterenko, M.P. Bondar, and I.V. Ershov, in "High-Pressure Science and Technology-1993," eds. S.C. Schmidt, J.W. Shaner, G.A. Samara, and M.Ross, AIP Press, NY, 1994, p. 1173.
10. V.F. Nesterenko and M.P. Bondar, DYMAT J., 1 (1994) 245.
11. R.W. Armstrong, in "Advances in Materials Research," Vol. 5, eds. R.F. Bunshah, Wiley-Interscience, NY, 1971, p.101.
12. F. J. Zerilli and R. W. Armstrong, J. Appl. Phys. 68 (1990) 1580.
13. C.L. Wittman, R.K. Garrett, J.B. Clark, and C.M. Lopatin, in "Shock-Wave and High-Strain-Rate Phenomena in Materials," eds. M.A. Meyers, L.E. Murr, and K.P. Staudhammer, M.Dekker, NY, 1992, p. 925.
14. U.R. Andrade, M.A. Meyers, K.S. Vecchio, and A.H. Chokshi, Acta Met. et Mat., 42(1994) 3183.
15. B. Derby, Acta Met. et Mat., 39 (1991) 955.
16. J. Gil Sevillano, P. van Houtte, and E. Aernoudt, Prog. Mater. Sci., 25 (1981) 69.
17. W. Köck and P. Paschen, J. of Metals, 41 (No. 10) (1989) 33.
18. D. Beckenhauer, P. Niessen, and P. Pick, J. Matls. Sci. 12 (1993) 449.
19. A. Mendelson, Plasticity: Theory and Application, Krieger, Malabar, Fl., 1968,
20. R. Vandermeer and W.B. Snyder, Jr., Met. Trans. A, 10A (1979) 103.
21. T. E. Mitchell and W. A. Spitzig, Acta Met., 13 (1965) 1169.
22. R. J. Asaro, Acta Metall. 27 (1979) 445.
23. M. A. Meyers, G. Subhash, B. K. Kad, and L. Prasad, Mech. of Matls., 17 (1994) 175.